A Bayesian Inversion for the Generation of Felsic Archean Crust

Jannitta T. Yao[1] (jannitta.yao.gr@dartmouth.edu)**, C. Brenhin Keller**[1] (brenhin.keller@dartmouth.edu)

[1]*Department of Earth and Planetary Sciences, Dartmouth College, 19 Fayerweather Hill Rd HB6105, Hanover NH 03755*

This non-peer reviewed preprint, submitted to EarthArXiv, has also been submitted to the *Geochemistry, Geophysics, Geosystems (G-cubed)* journal for peer review.

A Bayesian Inversion for the Generation of Felsic Archean Crust

Preprint, compiled July 2, 2026

Jannitta T. Yao [1*] **and C. Brenhin Keller** [1†]

[1]Department of Earth and Planetary Sciences, Dartmouth College

Abstract

Archean continental crust is compositionally distinct from post-Archean continental crust; its felsic components predominantly comprise the tonalite, trondhjemite, and granodiorite suite, while its mafic components record evidence of secular mantle cooling. Although the geochemistry of these rocks have been well characterized, the production of Archean felsic magmas remains contested because the early Earth's dominant geodynamic regime is uncertain. Here, a novel integration of parallel Markov chain Monte Carlo methods with the Perple_X thermodynamic forward model inverts for the H_2O content and the P–T evolution required of primitive magmas to generate differentiation trends recorded by the Archean igneous rock record. Resulting P–T paths show a period of extended differentiation at 4-5 kbar with a H_2O content of ~3.4 wt%. These results are consistent with the depth and water content of mantle-derived mafic magmas in modern arcs, and point towards subduction as a potential tectonic setting for the production of these magmas.

Submitted for publication in *G-cubed*

1 Introduction

The chemically evolved, andesitic bulk composition of Earth's continental crust is unique among the other rocky bodies of the Solar System [1]. The geochemistry of this crust has evolved through its 4.5 billion year history to reflect surface heat loss and the decrease in radiogenic heat-producing isotopes. Statistical analyses of the bulk rock record by [2] and [3] have shown a change in the major and trace element composition of continental crust over Earth history. Specifically, an observed change in major elements such as Na_2O and K_2O and in incompatible element ratios such as La/Yb and Eu/Eu* over the Archean-Proterozoic boundary are interpreted to correspond to mantle cooling and a change in global tectonics after the end of the Archean.

This change in crustal geochemistry from the Archean to modern continental crust is most prominently observed in the lithologies of Archean continental crust (Figure 1). Extant felsic Archean crust is distinctly different from modern felsic crust. Preserved Archean crust makes up ~5% of Earth's crust and are mostly comprised of "granite-greenstone terranes", greenstone belts that are intruded by granitic gneisses [4, 5]. The mafic metavolcanic greenstone belts contain komatiites and pillow basalts and are interpreted as fragments of preserved oceanic crust. The felsic granitic gneisses make up the majority (85-90%) of extant Archean crust and are mostly compositionally classified as trondhjemites, tonalites, and granodioties (TTGs) [6]. Felsic Archean crust is distinctly sodic (3-7 wt% Na_2O; [7, 8]) when compared to modern felsic crust (~3.27 wt%; [9]).

While experimental data and thermodynamic modeling have shown that TTG melt can be produced from the partial melting of metamafic rocks at mid-to-lower crustal pressures (depth ≥ 50 km), the tectonic setting that produced these felsic magmas remains contested due to uncertainty surrounding the geodynamic regime of the Archean, the onset of global subduction, and the rate at which felsic Archean crust was produced [10, 11, 12]. Multiple mechanisms have been proposed for the geodynamic regime, including stagnant lid and mobile lid (active plate tectonics) as two potential end members. Proposed tectonic mechanisms for the generation of Archean continental crust involving a stagnant lid regime include "sagduction" and basal melting of a thick mafic crust or slab melting of oceanic crust, and subduction for a mobile lid regime [13, 7, 14]. Additionally, understanding the geochemical evolution of Earth's crust is also important in the context of global climate because the strength of the silicate weathering feedback, the primary mechanism of regulating temperature on geologic timescales, depends on the abundance of subaerial continental crust [15]. Therefore, constraining the conditions in which Archean felsic crust formed will improve understanding of the geodynamic regime that formed Earth's earliest continents as well as planetary evolution and habitability.

Decades of research on TTG and other Archean granitic crust has resulted in thorough study of the major and trace element geochemistry of Archean felsic crust [11, 8]. Together with statistical analyses such as weighted bootstrap resampling, it is possible to quantitatively characterize Archean felsic differentiation trends in substantial detail [3]. These bulk differentiation trends present a compelling inverse problem, where calculating the conditions that produced these differentiation trends can lead to further insight on the genesis of these felsic magmas. To that end, this paper describes a novel Bayesian inversion that integrates parallel Markov chain Monte Carlo (MCMC) methods with the Perple_X thermodynamic forward model to solve for the possible range of P–T paths and starting H_2O compositions through which sequential fractionation and equilibrium melt differentiation may produce the observed differentiation trends preserved in Archean continental crust.

2 Method Development

2.1 *Observed Archean Differentiation Trends*

The inverse model solves for the H_2O content of the primitive magma and the P–T paths of the melt evolution required to produce the differentiation trends observed in preserved Archean crust. These differentiation trends are compiled from the EarthChem database, as well as the compilations of [16] and [17], as in [3]. To address the inherent issue of spatiotemporal bias

*correspondence: jannitta.yao.gr@dartmouth.edu

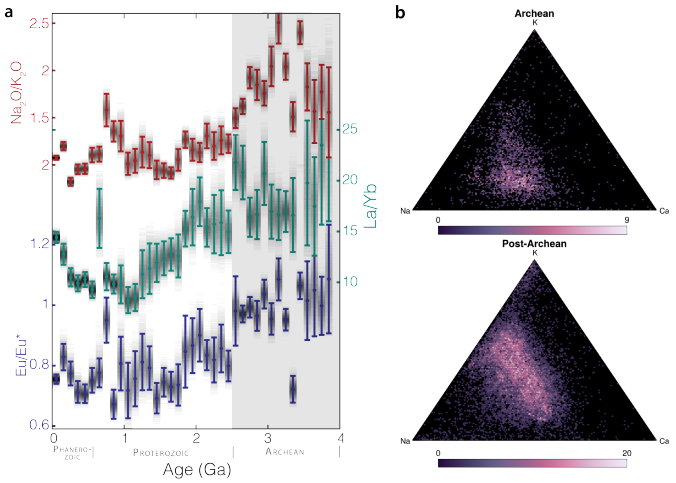

Figure 1: a: Geochemical trends of Na_2O/K_2O, La/Yb, and Eu/Eu* in felsic (62-73 wt% SiO_2) rocks over time, with the Archean Eon highlighted in the grey box. From [3]. b: Ca, Na, and K ternary histograms of the same data, split between Archean and post-Archean samples.

in Archean crustal sampling, data points are calculated using a weighted bootstrap resampling technique after [3], where weights are inversely proportional to the spatiotemporal density of the data. Data points are then bootstrap resampled based on their assigned weights, with synthetic datasets created from a Gaussian distribution with a mean and standard deviation based on the original mean and uncertainty of the original data point, and then sorted into 100 Ma time bins.

2.2 *Perple_X Forward Model*

The Perple_X thermodynamic modeling software is an open-source, Gibbs free energy minimization program that calculates the most stable phases of a given composition for a range of pressures and temperatures through the linear approximation of solution series by a discrete set of pseudocompounds [18, 19]. Perple_X uses an internally consistent thermodynamic dataset to calculate the stability of pure phases, along with solution models for melt and solid phases with continuously variable compositions. The thermodynamic dataset, melt model, and other solution phase models are specified by the user from a selection of published thermodynamic models calibrated by experimental petrology. Perple_X performs Gibbs free energy minimization through linear optimization by representing the composition variation of the phases of interest as a set of linear "pseudocompounds".

For this model, the chemical system is defined as the SiO_2 – TiO_2 – Al_2O_3 – FeO – MgO – CaO – Na_2O – K_2O – H_2O – O_2 melt system. The thermodynamic dataset is set to version 6.3.3 of the Holland Powell thermodynamic dataset [20], with the "igneous" set of solution models as specified by [21] for melt, aqueous fluid, spinel, garnet, olivine, orthopyroxene, clinopyroxene from [21], plagioclase from [22], epidote from [20], cordierite, chlorite, muscovite, and biotite from [23], hornblende from [24], and ilmenite from [25]. The bulk composition of the primitive magma is set to the composition of the major elements in the first SiO_2 bin of the Archean differentation trends from the dataset compiled by [3], which represents an average Archean basaltic composition. These forward model runs are automated through StatGeochem.jl, an open-source package which provides a programmatic interface for Perple_X model runs [26] in the Julia programming language [27].

Perple_X models the stability of minerals in equilibrium with a melt across varying pressure and temperature conditions. In one of the simplest cases, that of varying temperature along an isobar, this is equivalent to modelling minerals crystallizing out from magma during cooling in a closed-system magma chamber. Realistically, magmas within Earth's crust undergo open-system processes such as fractional crystallization, where a fraction of the magma is physically and chemically separated from the cumulate solid. To simulate these processes, a stepwise fractional crystallization process has been implemented that simulates the extraction and ascent of melt through a series of magma chambers, where isobaric equilibrium crystallization is occurring at each magma chamber, and the P–T path of this process is represented by a series of isobaric paths that decrease in temperature. After each isobar, the composition of the melt phase is set as the starting bulk composition of the next isobar to simulate melt extraction.

Trace element partitioning is additionally calculated based on equilibrium paritioning equations along with partition coefficients derived from the Geochemical Earth Reference Model (GERM) database of experimentally determined trace element partition coefficients. These partition coefficients, as provided in StatGeochem.jl, are averaged from the GERM compilation and bootstrap resampled as a function of bulk silica. For each trace element, a bulk partition coefficient is then calculated from the solid phase output from Perple_X with the following equation:

$$\bar{D}_i = \Sigma W_A D_i^A \tag{1}$$

where W_A is the weight percent of mineral A in the rock and D_i^A is the partition coefficient of element i in mineral A. This bulk partition coefficient is used to calculate trace element partitioning between the melt and the solid. A selection of trace element partition coefficients for major and accessory phases can be found in Supplementary Figure 1.

Accessory phase saturation is calculated using experimentally determined saturation equations for apatite [28], zircon [29], sphene [30], and monazite [31]. After accessory phase saturation, the bulk partition coefficient is recalculated based on all solid phases, including accessory phases. Melt composition is recalculated from these partition coefficients, adjusting for any elements that are limited by saturation.

2.3 *Bayesian Inverse Model*

Markov chain Monte Carlo (MCMC) methods are based in Bayesian statistics and use repeated sampling in the form of a Markov chain to obtain samples from a posterior distribution which could not otherwise be sampled directly. For example, given a forward model which takes as input some parameters of interest and yields as output some quantities which can be compared to observed data, the posterior distribution may be the distribution of those parameters of the forward model, given the observed data. In the simplest case, such Markov chains may be

constructed using the Metropolis algorithm, which determines the probability of acceptance of a new proposal (including the values of any parameters of the forward model) based on the ratio of the likelihood of the new proposal to that of the last accepted proposal [32]. After an initial "burn-in" period where the model explores the parameter space, the Markov chain will reach a stationary distribution such that each successive node represents a draw from the posterior distribution of interest. In order to reduce the amount of burn-in time, the model will also be parallelized using the process of replica exchange (section 2.5), after [33].

A MCMC approach for the model inversion is tolerant of substantial prior uncertainty regarding the values of the parameters of interest; given sufficient time for burn-in, the inverse model can explore even a large parameter space and converge at an accurate posterior distribution. The provided priors present such a parameter space, with H_2O represented as a uniform distribution from 0.05 to 15 wt%, and P and T ranging from 1 to 20000 bar and 550 to 1550 °C, respectively. The jumping distributions that are used to propose new candidates are symmetric Gaussian distributions for both H_2O, P, and T, with a standard deviation of 1 for H_2O and a standard deviation equal to 1/60th the possible range for P and T. The candidate set of (P, T) pairs represent a monotonically decreasing sequence of isobaric equilibrium differentiation pressures and temperature changepoints. For each model run, a new candidate set is proposed by perturbing a randomly selected (P, T) pair from the previously accepted set. The stationary distributions of each of the Markov chains will represent the posterior distributions of the P–T paths and H_2O of magma differentiation in the Archean where each accepted proposal in the Markov chain represents a Perple_X forward run.

2.4 *Calculating likelihood and accounting for covariance*

New proposals are generated by perturbing the current accepted proposed values through a jumping distribution. The likelihood of each new proposal is calculated based on how well the Perple_X outputs describe the geochemical differentiation trends recorded in Archean felsic crust. The likelihood is calculated from the sum of the multivariate Gaussian probability density function (PDF) of the major and trace elements in each silica bin (53-72 wt% SiO_2, split into 14 bins). Trace element likelihood is calculated using a multivariate Gaussian PDF for the distribution of the logarithm of trace element concentration, to account for the characteristically log-Normal distribution of trace elements. The multivariate Gaussian PDF includes a covariant matrix to account for the inherent interdependencies between elements (Supplementary Figure 2):

$$(2\pi)^{-k/2} det(\Sigma)^{-1/2} exp(-\frac{1}{2}(x-\mu)^T \Sigma^{-1}(x-\mu)) \qquad (2)$$

where Σ is a covariant matrix and μ and x are vectors.

The likelihood for the new set of proposed values is accepted based on the ratio of the probabilities between the new proposal and the current accepted proposal.

2.5 *Parallelization*

The model is parallelized on the San Diego Supercomputing Center Expanse cluster with the replica exchange process [35].

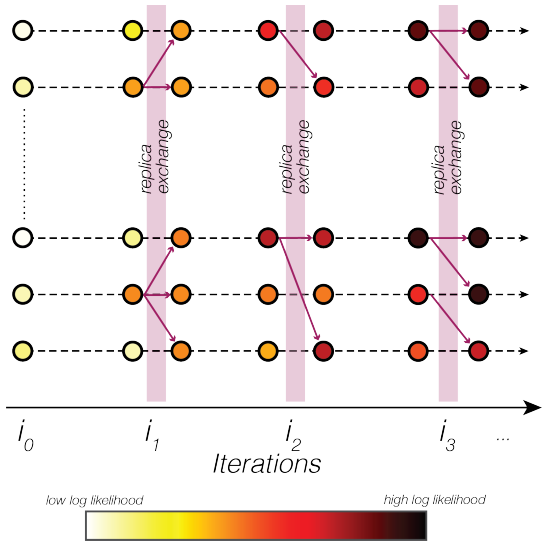

Figure 2: Schematic of replica exchange MCMC. In a parallel system, all of the cores connected with dashed lines represent the system after each forward model run. Cores are filled in depending on the log likelihood of their current proposal. Pink vertical bars show the process of replica exchange for each model iteration, with swapped states. Pink arrows represent the exchange that happens at every step. Modified from [34].

The replica exchange process reduces the burn-in time that is characteristic of MCMC methods (Figure 2). In replica exchange, cores communicate with each other after each Perple_X run to compare likelihoods using the MPI.jl package [36]. Cores will copy the set of proposed values from another core if that core has a higher likelihood. All cores communicate with and see the likelihoods of every other core in the system. Replica exchange is performed every 5 steps. From an efficiency point of view, the communication overhead inherent to the blocking message passing interface methods is negligible relative to the time it takes to run the Perple_X forward model. Strong scaling tests from [33] demonstrate that the replica exchange model, given the minutes-long Perple_X forward model runs, maintains near-linear speedup until the core count is increased by several orders of magnitude beyond the current configuration.

3 RESULTS AND DISCUSSION

3.1 *Equilibrium distributions of H_2O, P, and T*

The log likelihood of accepted proposals provides a quantitative measure of how well the Perple_X outputs match the Archean geochemical differentiation trends. Figure 3 shows the evolution of the log likelihoods and the initial H_2O content across all 128 cores on 1132 Perple_X runs per core. Model convergence is a qualitative assessment of the variance of the log likelihood of accepted proposals, and of the variance of the Markov chains for H_2O and P–T conditions. From these data, convergence is assessed to begin after ~200 steps of the parallel Markov chain based on the sharp increase in log likelihood from an initial value of -8×10^{-5} to an equilibrium range of -28000 to -25600. The H_2O Markov chain correspondingly shows a convergence around 200 model steps from an initial set of values that range

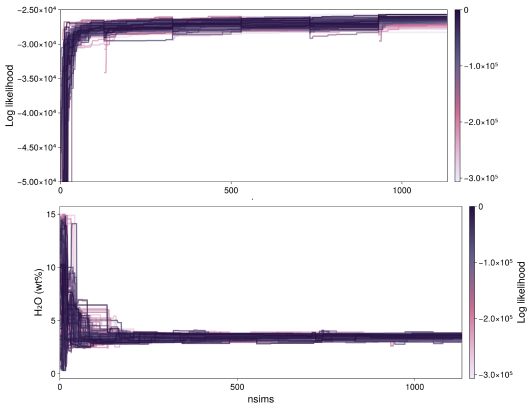

Figure 3: Parallel Markov chains for log likelihood (top) and primitive magma H_2O (bottom) of melt in the currently accepted proposal as a function of the number of Metropolis steps taken. Each line represents a single core, with 128 total cores shown. The primitive bulk H_2O concentration appears to converge after ~200 parallel steps of the Markov chain, coincident with the plateauing of the log likelihood of accepted proposals.

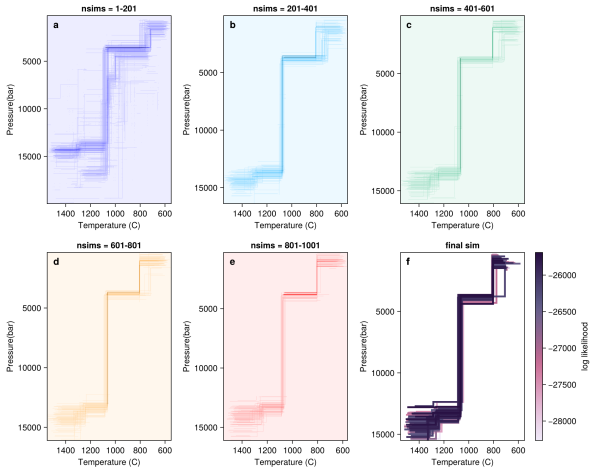

Figure 4: Heatmaps (a-e) depicting the convergence of P–T paths of melt over 1000 model runs. Final melt P–T paths (f) across all 128 cores are plotted and colored by log likelihood. P–T paths appear to converge after ~200 parallel steps of the Markov chain (b-e), coincident with the plateauing of the log likelihood of accepted proposals.

from 0.01 to 15 wt% to a much tighter range of 3.0-3.8 wt%. The convergence of the P–T paths for melt is shown in Figure 4. Similar to the Markov chains for log likelihood and H_2O, P–T convergence starts at around 200 model steps. The final model run of the melt P–T paths (Figure 4f) cut off once the solidus is reached, whereas the heatmaps (Figure 4a-e) show the entire range of the proposed paths. The changepoints recorded by the final melt P–T paths are identical to those of the stationary distribution (Figure 4b-e), so the final melt P–T paths are an accurate reflection of the stationary distribution.

The equilibrium distributions of the primitive magma H_2O content, the isobaric equilibrium differentiation P, and the T of the changepoints of the isobaric differentiation steps demonstrate the model's ability to resolve these parameters given that for all of these quantities, their posterior distributions are markedly lower in variance than the respective priors. The modalities of the equilibrium distributions (Figure 5) provide insight on the relative role of each parameter on the model output. The H_2O stationary distribution appears almost Gaussian, in comparison to the bimodal stationary distribution of the isobaric equilibrium differentiation pressures, or the more uniform distribution of the temperature changepoints. That is to say, the model converges on a single initial bulk H_2O of 3.6 wt%, but requires polybaric differentiation, while temperature of changepoints varies the least from the prior. In part, this points towards the importance of the bulk composition in magma differentiation. The importance of water in the differentiation trends of magmas has been well documented (i.e. [37, 38]), and as demonstrated by the equilibrium distribution, the average differentiation trends of Archean magmas require a specific amount of water in the starting bulk composition. Differentiation pressure plays a secondary role, and no single pressure fully explains the observed differentiation trends. The temperature of changepoints (at which fractionation and magma ascent occurs) plays the smallest role and accordingly has the least well resolved posterior distribution.

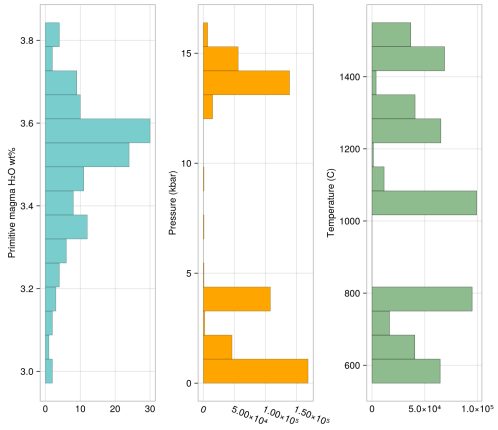

Figure 5: Equilibrium distribution histograms of the H_2O content of the primitive magma and the P and T of the changepoints in the P–T paths.

3.2 *Major and trace element evolution*

The inversion is able to fit Perple_X outputs with Archean crustal trends reasonably well to first order, with the major elements of melt from the Perple_X output (Figure 6) generally exhibiting better matches than the partitioning-based model for trace element concentrations (Figure 7). Harker diagrams comparing the melt composition from the final simulation of the Perple_X output across all 128 cores with the Archean crustal differentiation trends for major and trace elements are shown in figures 6 and 7. Similar to the P–T evolution (Figure 4), the final simulation of the Perple_X output across all cores appears to provide an accurate snapshot of the stationary distribution, so only these lines are shown for simplicity and ease of interpretation.

Within the major element trends, the slopes of the differentiation trends are captured by the Perple_X output. As expected, the

Perple_X output for mafic elements Mg, Fe, and Ca decrease and the felsic elements Al, K, and Na increase as Si increases. However, there are still some deviations between the EarthChem data and the Perple_X output. Notably, the Perple_X outputs of the melt Al_2O_3 evolution from 55-65 wt% SiO_2, the melt TiO_2 evolution from 53-60 wt% SiO_2, and the melt MgO evolution from 53-62 wt% SiO_2 show deviations from the EarthChem data of 0.5-3 wt%.

These deviations can be understood in terms of the evolution of the major and accessory mineral phases within the Perple_X model results (Figure 8). The sharp dip in MgO and the jump in Al_2O_3 can be attributed to the 15 wt% of clinopyroxene that is immediately crystallized from the basaltic starting composition. The continuous crystallization of pyroxene throughout the melt evolution contributes to the overall depression in the slope of Mg, Fe, and Ca. The inflection point and change in slope of Al_2O_3 at 65 wt% melt SiO_2 corresponds to the growth of amphibole at ~54 wt% melt SiO_2. Finally, the initial increase in the Perple_X output of TiO_2 relative to that of the EarthChem data is interpreted to result from the lack of stability of the accessory phase sphene (titanite).

Archean trace element differentiation trends are captured by the Perple_X output with varying levels of accuracy. The differentiation patterns of the HREE (i.e., Dy, Yb, Lu) and some of the LREEs (Sm, Nd) are relatively flat in logarithmic space, and the Perple_X output matches the slope of these data. Larger differences exist for the LREEs La and Ce, as well as for Ta, Th, Ba, and Cr. Some of these mismatches can be explained by major phase fractionation, such as the onset of clinopyroxene fractionation at 55 wt% melt SiO_2, which strongly partitions Cr, or feldspar fractionation from 56-72 wt% melt SiO_2, which partitions Ba.

Some potential underlying causes for such mismatches between observed and model differentiation trends are discussed in Section 3.4. First and foremost, it must be noted that the inversion is modeling an average Archean differentiation trend. The results from fitting these parameters to the average differentiation trend are conceptually distinct from those that would result from averaging the P–T–H_2O conditions of all individual local or regional Archean differentiation trends. Moreover, neither approach should necessarily be expected to capture the full realm of possible crustal differentiation conditions. Instead, it may be more accurate to consider that these results represent at least one possible way to produce Archean-like crust with the correct bulk compositions and covariance structure.

Despite these observed mismatches between the Perple_X output and the differentiation trends, the model has managed to reproduce these differentiation trends to the first order, which we consider a promising sign given the small number of variables (P, T, H_2O) that can be modified in our inversion compared to the large number of variables being fitted (i.e., 30+ major and trace elements, each with observations spanning 15 silica bins, as well as the covariances thereof). Of the several aspects of the model that are fixed (i.e. forced decrease in T, complete fractionation of melt from solid phases, fixed starting composition), the success of the model in replicating these trends can be largely attributed to the process of stepwise bulk fractionation as a model for the petrogenesis of felsic magmas. Prior iterations of this model that considered only batch crystallization occurring along a single isobar without melt fractionation resulted in larger mismatches between the Perple_X output and the differentiation trends, further underlining the importance of polybaric differentiation to our inversion results.

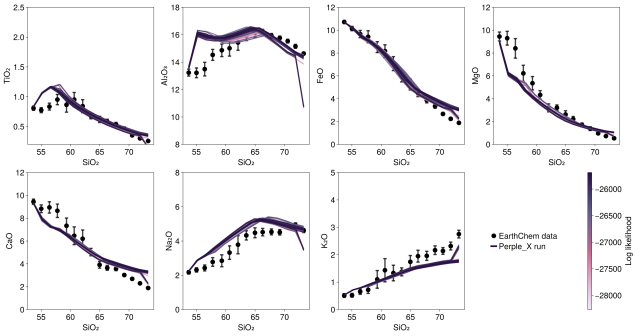

Figure 6: Harker diagrams comparing the differentiation trends between observed Archean felsic rocks and Perple_X outputs for the major elements of melt. Trends are binned by SiO_2. Each line represents a core and lines are colored by their likelihood.

3.3 Accessory phase saturation calculations

While not modeled by Perple_X directly, we additionally model the accessory phases apatite, zircon, sphene, and monazite by combining the Perple_X melt composition output with experimentally determined saturation equations and partition coefficients. In our inversion results, apatite (0.01-0.2 wt%), zircon (0.001-0.004 wt%), and monazite (0.001-0.006 wt%) saturation occur at felsic melt compositions where SiO_2 > 60 wt%. Of these 4 accessory phases, apatite is the only one that crystallizes at intermediate melt compositions. Zircon and monazite both only crystallize from high silica (SiO_2 > 75 wt%) melts. Monazite is not included in figure 8 given that in our forward models the crystallization of monazite only occurs at very high melt SiO_2 levels (SiO_2 > 77 wt%) outside of the range the inverse model considers. These results for zircon are consistent with the trend expected given zircon saturation modelling by [39], who found that zircon are less likely to crystallize from low-silica Archean magmas compared to low-silica modern magmas due to lower Zr abundances in Archean magmas. A primary control on accessory phase saturation is the abundance of incompatible minor-to-trace elements (i.e. Zr for zircon and baddeleyite; P for apatite, monazite, and xenotime), which have generally increased in abundance through time as a result of secular mantle cooling and decreasing average mantle melting extent (Figure 9; [3]). Sensitivity tests of zircon and apatite saturation show that crystallization occurs from lower silica melts with a higher initial abundance of Zr and P, respectively (Supplementary Figures 3 & 4). Similarly, sensitivity tests of sphene saturation, which isn't crystallizing under current conditions, also show that the initial TiO_2 content of ~0.8 wt% is not high enough to result in sphene saturation (Supplementary Figure 5). Comparisons of average differentiation trends through time show an increase in TiO_2 after the Archean as well (Figure 9). Therefore, the low abundances of these accessory phases can be attributed to the lower abundances of both major and trace elements in the Archean.

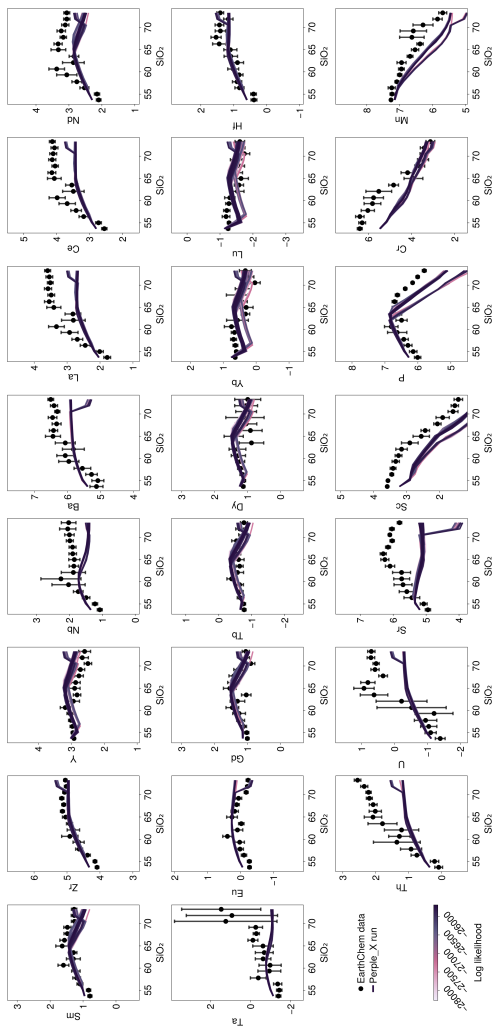

Figure 7: Harker diagrams comparing the differentiation trends between observed Archean felsic rocks and Perple_X outputs for the trace elements of melt. Trace element concentrations are shown in log space. Each line represents a core and lines are colored by their likelihood.

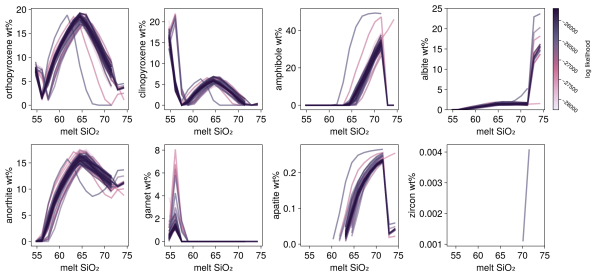

Figure 8: Phase evolution plots showing wt% of major phases as melt evolves. Each line represents a single core, and lines are color-coded by likelihood.

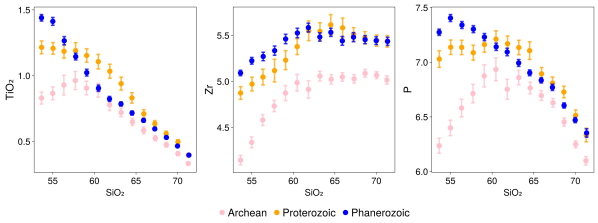

Figure 9: TiO_2, Zr, and P (in wt%) differentiation trends during the 3 geologic eons, binned by SiO_2. Zr and P are plotted in log space.

3.4 Model Limitations

3.4.1 Geologic complexity

One shortcoming inherent in most all attempts at modeling Earth processes is the scale of geologic complexity, which can rarely if ever be fully represented in forward models. For example, while we implemented manual melt fractionation (see Section 2.2) in an attempt to simulate melt fractionation in a magma chamber, limitations remain with this design. The number of times the melt was fractionated is constrained by the number of isobaric differentiation paths run by Perple_X, which is limited to 5 in our present inversion. Additionally, each isobaric path in Perple_X undergoes batch crystallization (i.e., equilibrium crystallization), restrcting any fractionation to the end of each isobaric path. While stepwise differentiation across small increments of P-T space can approximate fractional crystallization by effectively resetting the bulk composition at each step, this approach introduces its own assumptions about the degree of melt-solid separation that occurs during fractional crystallization, and remains a discrete approximation of what is likely in nature a near-continuous process. More complex magmatic processes like magma mixing and assimilation are also not represented in this model.

3.4.2 Trace element partition coefficient limitations

Trace element partition coefficients are compiled based on the GERM Kd database of experimentally determined trace element partition coefficients using StatGeochem.jl [26]. These partition coefficients are interpolated as a function of melt SiO_2, and applied to the modelled stable major and accessory phases given the Perple_X model melt SiO_2 and melt fraction. Mineral/melt partition coefficients for each phase in the stable assemblage are averaged from individual entries for experimentally determined mineral/melt partition coefficients and summed together. These partition coefficients from GERM Kd are not constrained by P/T or other thermodynamic conditions, except to any degree that these may correlate with melt SiO_2, meaning that the averaged partition coefficients implicitly incorporate experimental data collected across a broad range of conditions that may not reflect the conditions explored by the forward model.

3.4.3 Thermodynamic equilibrium

The assumption of equilibrium poses a central limitation for all thermodynamic forward models, a limitation which the field of petrologic modeling as a whole must frequently grapple with (i.e., [40]). The condition of phase equilibrium, where the chem-

ical potentials of all phases are equal, must be fulfilled in Perple_X's calculation of the compositions and amounts of phases stable at a certain pressure and temperature. As such, these models assume local equilibria in a closed system at any given step, so can only approximate open system behaviors such as variable fractionation and melt extraction [41].

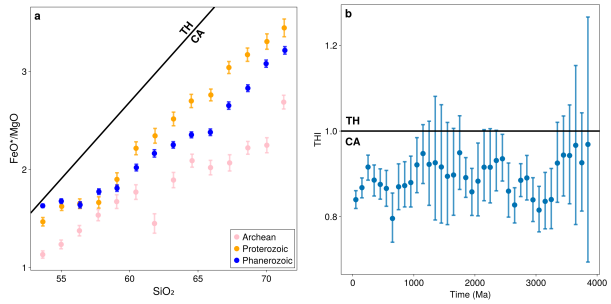

Figure 10: a. FeO*/MgO–SiO_2 of the 3 geologic eons, binned by SiO_2 wt%, with the tholeiitic/calc-alkaline dividing line from [42]. b. The tholeiitic index (THI) from [38] for igneous rocks (53 wt% < SiO_2 < 72 wt%), binned and resampled by age.

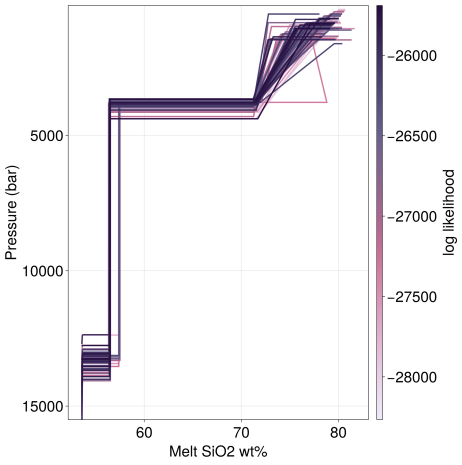

Figure 11: Evolution of the SiO_2 wt% of melt compared to the pressure (in bar) for final melt paths across all 128 cores. Most of the melt differentiation (55-72 wt% SiO_2) occurs at 4-5 kbar.

3.5 Implications for Archean tectonics

An initial value of ~3.6 wt% H_2O in the mafic parental magma is consistent with the average water content of mantle-derived, mafic magmas in modern volcanic arcs [37]. This relatively high H_2O content can explain how the average FeO*/MgO differentiation trends of the Archean, Proterozoic, and Paleozoic eons all fall largely within the calc-alkaline field, and how the mean tholeiitic index (THI) of igneous rocks through time is also predominantly calc-alkaline (Figure 10). Melt differentiation occurs at 3 main crustal depths: at 13-15 kbar (~46.8-54 km), at 4-5 kbar (~14.4-18 km), and at 0.5-2 kbar (~1.8-7.2 km) with the bulk of the differentiation occurring at 4-5 kbar, or in the mid-crust (Figure 11). These pressure conditions and the high water contents are broadly consistent with subduction at relatively shallow depths in an arc setting as a potential tectonic setting for the production of these magmas.

Within an Archean arc setting, differentiation by both partial melting and fractional crystallization may in principle occur under a wide range of conditions. One particular scenario that has been extensively discussed is slab melting [7]. Incompatible element similarities between Archean TTG and modern slab-derived adakites have been proposed as evidence for TTG magma genesis through slab melting [43]. [44] showed that at the elevated mantle temperatures of the Archean, downgoing slabs facing increased resistance from plate boundaries may have produced TTG magmas at depths of 35-45 km (9.7-12.5 kbar). Alternatively, [45] argued for Archean slab melting of oceanic plateau basalts under "hot subduction" conditions (>15 kbar). While our results suggest within-crustal differentiation, the pressures likely expected in a slab melting scenario (>10 kbar) exceed the supported range of most of the thermodynamic solution models upon which we rely. Consequently, while our model suggests polybaric differentiation primarily at within-crustal pressures, we cannot directly test the possibility of a slab melting contribution as a result of these limitations.

A purely stagnant-lid regime, where magmatism is dominated by internal overturn, delamination, and plume-driven melting mechanisms with limited transport of surface volatiles to mantle source regions, can not on its own explain the generation of consistently hydrous magmas. Sagduction of the base of thickened continental crust has been proposed as an alternative mechanism to subduction in a vertical tectonics-dominated regime, but [46] showed that sagduction produces water-poor, "dry" magmas that are unable to produce large enough volumes of melt with the composition of Archean granitoids. Geodynamic regimes involving lateral transport and vertical tectonics, such as a partially stagnant lid with localized subduction, or an active-lid regime with sustained subduction, are more compatible with our results.

While our estimate of 4 wt% water in Archean magmas representing the starting point of crustal differentiation, along with previous geochemical constraints such as THI are indicative of a similar proportion hydrated flux melting in the Archean, our geochemical results do not require that Archean tectonics were identical to modern plate tectonics. In particular, our results place no constraint on the timing or continuity of magmatism and crustal growth. In particular, this does not rule out models where magmatism may occur in several sharp pulses with periods of quiescent crustal growth [47, 48]. Paleomagnetic data of the Pilbara and Kaapvaal cratons show differential horizontal plate motion potentially compatible with an episodically mobile lithosphere [49]. One constraint on this episodic growth model is the tholeiitic index (THI) of igneous rocks over time (Figure 10b; [38]), which suggest that the proportion of flux and decompression melting stays relatively stable through the Archean. Regardless, our results do not distinguish between episodic overturning of the lithosphere and punctuated periods of crustal growth and active-lid, consistently mobile plate tectonics. These results should thus be considered a reflection of the dominant tectonic setting during periods of active magmatism, rather than the single, globally uniform tectonic regime of the Archean Eon as a whole.

4 CONCLUSIONS

Our parallel Bayesian inverse model solves for the parental magma water content and the P–T conditions of the melt evo-

lution required to produce the average differentiation trends recorded in Archean felsic rocks. The parallelization of this model uses a replica exchange approach to distribute the bottleneck of running the Perple_X thermodynamic forward model, and is able to explore a wide range of possible candidates for H_2O and P-T while simultaneously reducing the number of sequential Perple_X runs needed to reach an equilibrium state in any one of the parallel Markov chains.

This model can be applied to differentiation trends through time to better understand the evolution and petrogenesis of continental crust. In principle, this model may be used to invert for the parental magma water content and the P–T conditions of the melt evolution for a sufficiently large and representative whole-rock sample set from any geologic setting that records a magmatic differentiation process. Adjusting the efficiency of fractionation or simulating magma mixing between two parental magmas may also improve the range of geologic complexity that this model covers.

Our findings show that the parental magmas were hydrous (~3.6 wt% H_2O) with most differentiation occurring in the mid-crust (4-5 kbar). The equilibrium distributions of H_2O and the P/T of the changepoints of the differentiation steps highlight the importance of water in magma evolution, with the initial value of ~3.6 wt% H_2O proving to be comparable to water contents of primitive waters in modern arcs. These results strongly favor a tectonic regime capable of recycling surface-derived water into magma source regions, and are therefore inconsistent with a purely stagnant-lid Earth. Instead, they point to subduction-like processes as a key mechanism of crust formation.

ACKNOWLEDGEMENTS

This work used the Expanse cluster at the San Diego Supercomputer Cluster through allocation EES240071 from the Advanced Cyberinfrastructure Coordination Ecosystem: Services & Support (ACCESS) program, which is supported by U.S. National Science Foundation grants 2138259, 2138286, 2138307, 2137603, and 2138296. This work was supported by a NSF Graduate Research Fellowship 2236868 awarded to J.Yao.

REFERENCES

[1] I. H. Campbell and S. R. Taylor. No water, no granites - No oceans, no continents. *Geophysical Research Letters*, 10(11):1061–1064, November 1983. ISSN 00948276. doi: 10.1029/GL010i011p01061.

[2] Kent C. Condie and Craig O'Neill. The Archean-Proterozoic Boundary: 500 My of Tectonic Transition in Earth History. *American Journal of Science*, 310(9): 775–790, 2010. doi: 10.2475/09.2010.01.

[3] C. Brenhin Keller and Blair Schoene. Statistical geochemistry reveals disruption in secular lithospheric evolution about 2.5 Gyr ago. *Nature*, 485(7399):490–493, 2012. ISSN 0028-0836, 1476-4687. doi: 10.1038/nature11024.

[4] Irina M. Artemieva. Global 1× 1 thermal model TC1 for the continental lithosphere: implications for lithosphere secular evolution. *Tectonophysics*, 416(1-4):245–277, 2006. ISBN: 0040-1951.

[5] A. Y. Glikson. Early Precambrian tonalite-trondhjemite sialic nuclei. *Earth-Science Reviews*, 15(1):1–73, 1979. ISSN 0012-8252. doi: 10.1016/0012-8252(79)90043-6.

[6] K. C. Condie. *Archean Greenstone Belts*. Elsevier, January 1981. ISBN 978-0-08-086902-5. Google-Books-ID: 6LkEpT_nlOAC.

[7] Mark S. Drummond and Marc J. Defant. A model for Trondhjemite-Tonalite-Dacite Genesis and crustal growth via slab melting: Archean to modern comparisons. *Journal of Geophysical Research: Solid Earth*, 95(B13): 21503–21521, 1990. ISSN 2156-2202. doi: 10.1029/JB095iB13p21503.

[8] Jean-François Moyen and Hervé Martin. Forty years of TTG research. *Lithos*, 148:312–336, 2012. ISSN 00244937. doi: 10.1016/j.lithos.2012.06.010.

[9] R.L. Rudnick and S. Gao. Composition of the Continental Crust. In *Treatise on Geochemistry*, pages 1–51. Elsevier, 2014. ISBN 978-0-08-098300-4. doi: 10.1016/B978-0-08-095975-7.00301-6.

[10] Kent C. Condie and Keith Benn. Archean geodynamics: Similar to or different from modern geodynamics? 164: 47–59, 2006. doi: 10.1029/164GM05.

[11] Kent C. Condie. How to Make a Continent: Thirty-five Years of TTG Research. In Yildirim Dilek and Harald Furnes, editors, *Evolution of Archean Crust and Early Life*, pages 179–193. Springer Netherlands, Dordrecht, 2014. ISBN 978-94-007-7615-9. doi: 10.1007/978-94-007-7615-9_7.

[12] J. Moyen and Gary Stevens. Experimental constraints on TTG petrogenesis: implications for Archean geodynamics. *Geophysical Monograph-American Geophysical Union*, 164:149, 2006. ISBN: 0065-8448.

[13] Nicholas Arndt. How did the continental crust form: No basalt, no water, no granite. *Precambrian Research*, 397: 107196, 2023. ISBN: 0301-9268.

[14] Hugh Rollinson. Coupled evolution of Archean continental crust and subcontinental lithospheric mantle. *Geology*, 38 (12):1083–1086, 2010. ISSN 0091-7613. doi: 10.1130/G31159.1.

[15] James C. G. Walker, P. B. Hays, and J. F. Kasting. A negative feedback mechanism for the long-term stabilization of Earth's surface temperature. *Journal of Geophysical Research*, 86(C10):9776, 1981. ISSN 0148-0227. doi: 10.1029/JC086iC10p09776.

[16] Kent C. Condie, Elena Belousova, W. L. Griffin, and Keith N. Sircombe. Granitoid events in space and time: Constraints from igneous and detrital zircon age spectra. *Gondwana Research*, 15(3):228–242, June 2009. ISSN 1342-937X. doi: 10.1016/j.gr.2008.06.001.

[17] Jean-François Moyen. The composite Archaean grey gneisses: Petrological significance, and evidence for a non-unique tectonic setting for Archaean crustal growth. *Lithos*, 123(1-4):21–36, 2011. ISSN 00244937. doi: 10.1016/j.lithos.2010.09.015.

[18] James AD Connolly. Computation of phase equilibria by linear programming: a tool for geodynamic modeling and its application to subduction zone decarbonation. *Earth*

and Planetary Science Letters, 236(1-2):524–541, 2005. ISBN: 0012-821X.

[19] J. A. Connolly. jadconnolly/Perple_x, October 2022. URL https://github.com/jadconnolly/Perple_X.

[20] T. J. B. Holland and R. Powell. An improved and extended internally consistent thermodynamic dataset for phases of petrological interest, involving a new equation of state for solids. *Journal of Metamorphic Geology*, 29(3):333–383, 2011. ISSN 1525-1314. doi: 10.1111/j.1525-1314.2010.00923.x.

[21] Tim J B Holland, Eleanor C R Green, and Roger Powell. Melting of Peridotites through to Granites: A Simple Thermodynamic Model in the System KNCFMASHTOCr. *Journal of Petrology*, 59(5):881–900, 2018. ISSN 0022-3530, 1460-2415. doi: 10.1093/petrology/egy048.

[22] Tim Holland and Roger Powell. Activity–composition relations for phases in petrological calculations: an asymmetric multicomponent formulation. *Contributions to Mineralogy and Petrology*, 145(4):492–501, 2003. ISSN 1432-0967. doi: 10.1007/s00410-003-0464-z.

[23] R. W. White, R. Powell, T. J. B. Holland, T. E. Johnson, and E. C. R. Green. New mineral activity-composition relations for thermodynamic calculations in metapelitic systems. *Journal of Metamorphic Geology*, 32(3):261–286, 2014. ISSN 02634929. doi: 10.1111/jmg.12071.

[24] E. C. R. Green, R. W. White, J. F. A. Diener, R. Powell, T. J. B. Holland, and R. M. Palin. Activity–composition relations for the calculation of partial melting equilibria in metabasic rocks. *Journal of Metamorphic Geology*, 34(9):845–869, 2016. ISSN 1525-1314. doi: 10.1111/jmg.12211. URL https://onlinelibrary.wiley.com/doi/abs/10.1111/jmg.12211. _eprint: https://onlinelibrary.wiley.com/doi/pdf/10.1111/jmg.12211.

[25] White, Powell, Holland, and Worley. The effect of TiO2 and Fe2O3 on metapelitic assemblages at greenschist and amphibolite facies conditions: mineral equilibria calculations in the system K2O–FeO–MgO–Al2O3–SiO2–H2O–TiO2–Fe2O3. *Journal of Metamorphic Geology*, 18(5):497–511, 2000. ISSN 1525-1314. doi: 10.1046/j.1525-1314.2000.00269.x.

[26] C. Brenhin Keller. StatGeochem.jl: Computational tools for statistical geochemistry and petrology. 2021. doi: 10.17605/OSF.IO/TJHMW.

[27] Jeff Bezanson, Alan Edelman, Stefan Karpinski, and Viral B. Shah. Julia: A Fresh Approach to Numerical Computing. *SIAM Review*, 59(1):65–98, January 2017. ISSN 0036-1445, 1095-7200. doi: 10.1137/141000671.

[28] T. Mark Harrison and E. Bruce Watson. The behavior of apatite during crustal anatexis: Equilibrium and kinetic considerations. *Geochimica et Cosmochimica Acta*, 48 (7):1467–1477, 1984. ISSN 0016-7037. doi: 10.1016/0016-7037(84)90403-4.

[29] Patrick Boehnke, E. Bruce Watson, Dustin Trail, T. Mark Harrison, and Axel K. Schmitt. Zircon saturation re-revisited. *Chemical Geology*, 351:324–334, 2013. ISSN 0009-2541. doi: 10.1016/j.chemgeo.2013.05.028.

[30] John C. Ayers, Daniel Flanagan, Calvin Miller, E. B. Watson, F. J. Ryerson, Blake Wallrich, and Michael Ackerson. The solubility of titanite in silicate melt determined from growth and dissolution experiments. *Contributions to Mineralogy and Petrology*, 177(3):37, March 2022. ISSN 1432-0967. doi: 10.1007/s00410-022-01902-z.

[31] Jean-Marc Montel. A model for monazite/melt equilibrium and application to the generation of granitic magmas. *Chemical Geology*, 110(1):127–146, 1993. ISSN 0009-2541. doi: 10.1016/0009-2541(93)90250-M.

[32] Nicholas Metropolis, Arianna W. Rosenbluth, Marshall N. Rosenbluth, Augusta H. Teller, and Edward Teller. Equation of State Calculations by Fast Computing Machines. *The Journal of Chemical Physics*, 21(6):1087–1092, 1953. ISSN 0021-9606. doi: 10.1063/1.1699114.

[33] Alexander Cox and C. Brenhin Keller. A Bayesian inversion for emissions and export productivity across the end-Cretaceous boundary. *Science*, 381(6665):1446–1451, 2023. ISBN: 0036-8075.

[34] Alexander Cox and Brenhin Keller. A Bayesian Inversion for Emissions and Export Productivity Across the End-Cretaceous Boundary. Master's thesis, Dartmouth College, 2024. URL https://digitalcommons.dartmouth.edu/masters_theses/127.

[35] Timothy J. Boerner, Stephen Deems, Thomas R. Furlani, Shelley L. Knuth, and John Towns. ACCESS: Advancing Innovation: NSF's Advanced Cyberinfrastructure Coordination Ecosystem: Services & Support. In *Practice and Experience in Advanced Research Computing 2023: Computing for the Common Good*, PEARC '23, pages 173–176, New York, NY, USA, September 2023. Association for Computing Machinery. ISBN 978-1-4503-9985-2. doi: 10.1145/3569951.3597559.

[36] Simon Byrne, Lucas C. Wilcox, and Valentin Churavy. MPI.jl: Julia bindings for the Message Passing Interface. *Proceedings of the JuliaCon Conferences*, 1(1):68, July 2021. ISSN 2642-4029. doi: 10.21105/jcon.00068.

[37] Terry Plank, Katherine A. Kelley, Mindy M. Zimmer, Erik H. Hauri, and Paul J. Wallace. Why do mafic arc magmas contain 4wt% water on average? *Earth and Planetary Science Letters*, 364:168–179, 2013. ISSN 0012821X. doi: 10.1016/j.epsl.2012.11.044.

[38] Mindy M. Zimmer, Terry Plank, Erik H. Hauri, Gene M. Yogodzinski, Peter Stelling, Jessica Larsen, Brad Singer, Brian Jicha, Charles Mandeville, and Christopher J. Nye. The Role of Water in Generating the Calc-alkaline Trend: New Volatile Data for Aleutian Magmas and a New Tholeiitic Index. *Journal of Petrology*, 51(12):2411–2444, 2010. ISSN 0022-3530. doi: 10.1093/petrology/egq062.

[39] C. Brenhin Keller, Blair Schoene, and P. Boehnke. Temporal variation in relative zircon abundance throughout Earth history. *Geochemical Perspectives Letters*, 3(3):179–189, 2017.

[40] Frank S. Spear, Jay B. Thomas, and Benjamin W. Hallett. Overstepping the garnet isograd: a comparison of QuiG barometry and thermodynamic modeling. *Contributions to Mineralogy and Petrology*, 168(3):1059, 2014. ISSN 1432-0967. doi: 10.1007/s00410-014-1059-6.

[41] Mark S. Ghiorso. Thermodynamic Models of Igneous Processes. *Annual Review of Earth and Planetary Sciences*, 25(Volume 25, 1997):221–241, 1997. ISSN 0084-6597, 1545-4495. doi: 10.1146/annurev.earth.25.1.221.

[42] Akiho Miyashiro. Volcanic rock series in island arcs and active continental margins. *Amer. Jour. Sci.*, 274, 1974.

[43] Kent C. Condie. TTGs and adakites: are they both slab melts? *Lithos*, 80(1):33–44, March 2005. ISSN 0024-4937. doi: 10.1016/j.lithos.2003.11.001.

[44] Bradford J. Foley. Generation of Archean TTGs via sluggish subduction. *Geology*, 52(9):656–660, 2024. ISSN 0091-7613. doi: 10.1130/G52196.1.

[45] Hervé Martin, Jean-François Moyen, Martin Guitreau, Janne Blichert-Toft, and Jean-Luc Le Pennec. Why Archaean TTG cannot be generated by MORB melting in subduction zones. *Lithos*, 198-199:1–13, 2014. ISSN 0024-4937. doi: 10.1016/j.lithos.2014.02.017.

[46] Alberto Roman and Nicholas Arndt. Differentiated Archean oceanic crust: Its thermal structure, mechanical stability and a test of the sagduction hypothesis. *Geochimica et Cosmochimica Acta*, 278:65–77, 2020. ISSN 0016-7037. doi: 10.1016/j.gca.2019.07.009.

[47] Geoffrey F. Davies. Punctuated tectonic evolution of the earth. *Earth and Planetary Science Letters*, 136(3):363–379, 1995. ISSN 0012-821X. doi: 10.1016/0012-821X(95)00167-B.

[48] C.J. Hawkesworth, B. Dhuime, A.B. Pietranik, P.A. Cawood, A.I.S. Kemp, and C.D. Storey. The generation and evolution of the continental crust. *Journal of the Geological Society*, 167(2):229–248, 2010. ISSN 0016-7649. doi: 10.1144/0016-76492009-072.

[49] Alec R. Brenner, Roger R. Fu, Bradford J. Foley, Diogo L. Lourenço, Jasmine Palma-Gomez, Zheng Gong, Sarah C. Steele, Joanna Li, David T. Flannery, Adrian J. Brown, and Eben B. Hodgin. Paleomagnetic detection of relative plate motions and an infrequently reversing core dynamo at 3.5 Ga. *Science*, 391(6791):1278–1282, March 2026. doi: 10.1126/science.adw9250.

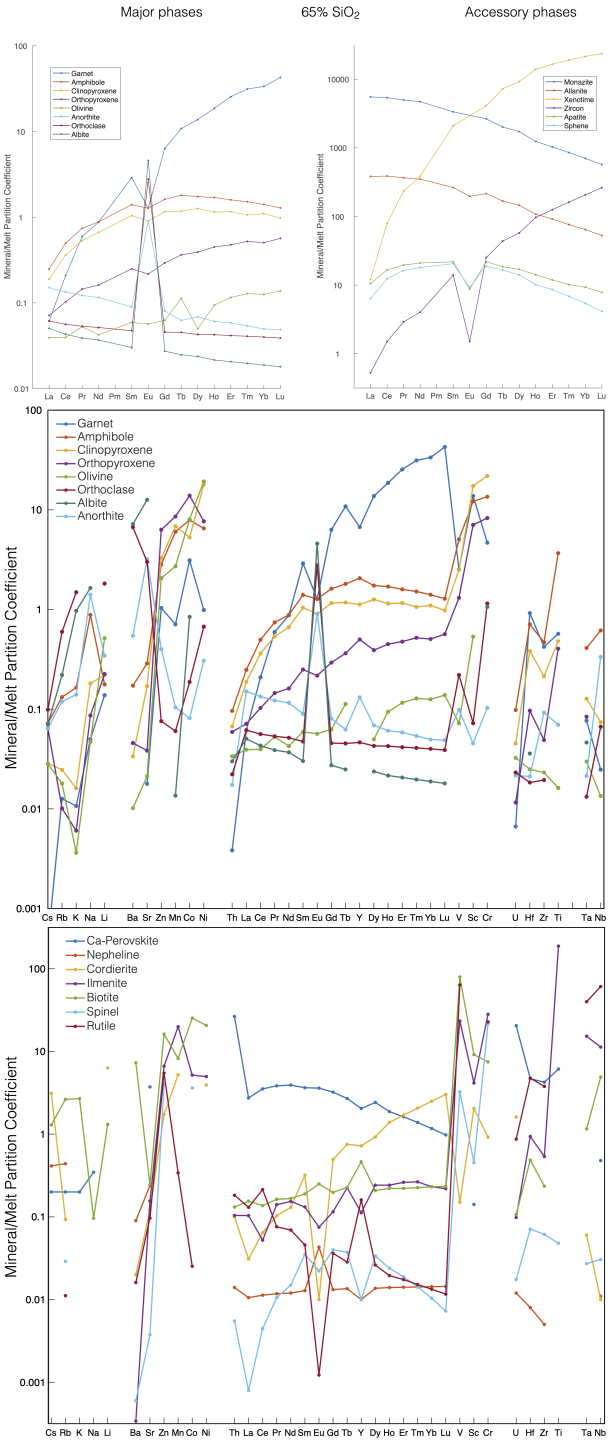

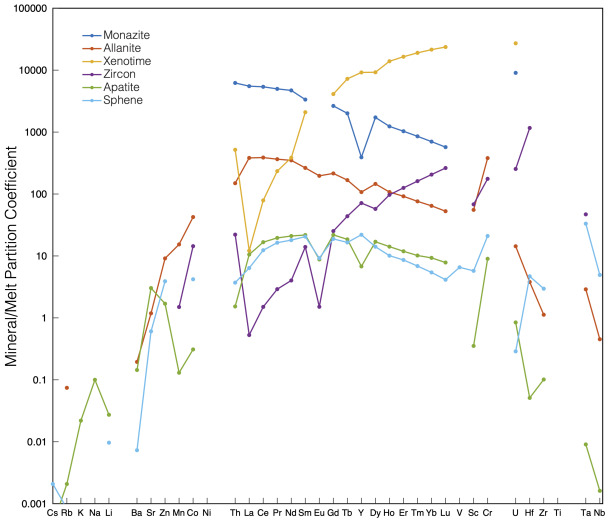

Supplementary Figure 1: Compilation of trace element partition coefficients for major and accessory phases from the GERM Kd database. All partition coefficients shown are for a felsic magma with 65 wt% SiO_2.

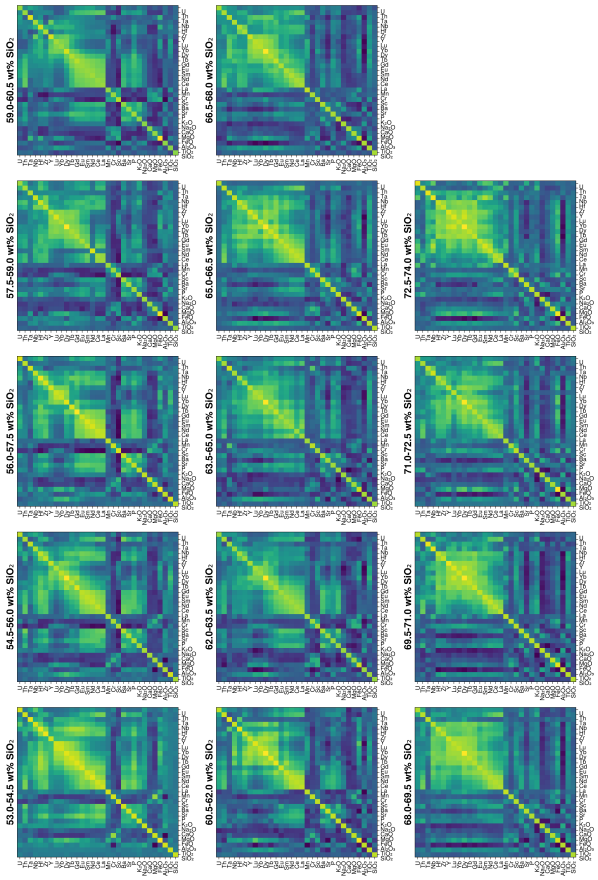

Supplementary Figure 2: Correlation matrices of major and trace elements for each SiO_2 bin shows interdependencies between elements.

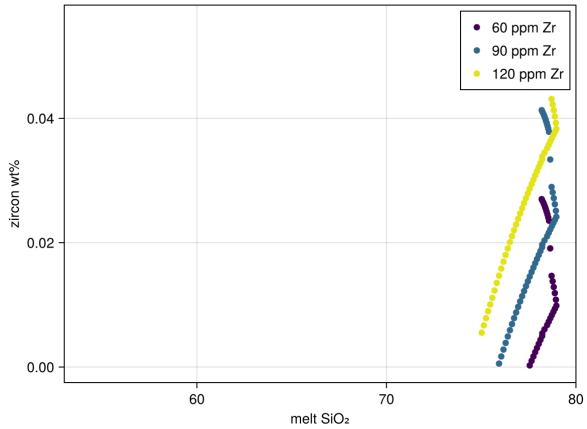

Supplementary Figure 3: Sensitivity tests of zircon saturation with a range (60-120 ppm) of Zr primitive magma compositions demonstrate that under the equilibrium H_2O and P–T conditions determined by the inverse model, zircon crystallizes from less felsic magmas with a higher Zr content in the primitive magmas.

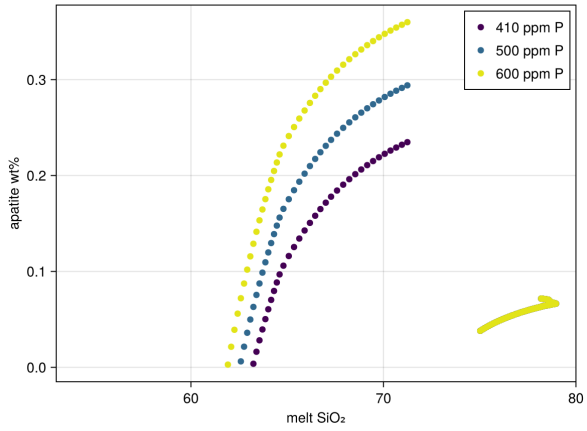

Supplementary Figure 4: Sensitivity tests of apatite saturation with a range (410-600 ppm) of P primitive magma compositions demonstrate that under the equilibrium H_2O and P–T conditions determined by the inverse model, apatite crystallizes from less felsic magmas with a higher P content in the primitive magmas.

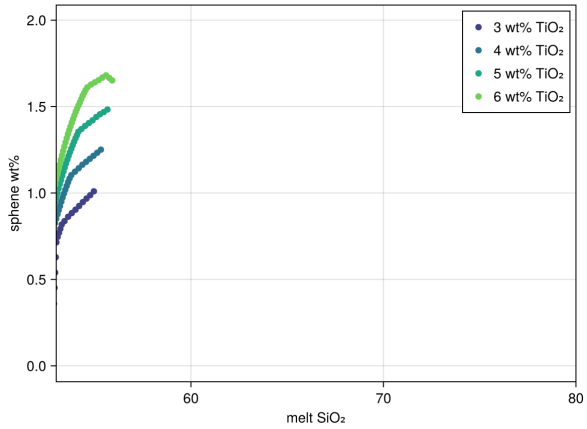

Supplementary Figure 5: Sensitivity tests of sphene saturation with a range (3-6 wt%) of TiO_2 primitive magma compositions demonstrate that under the equilibrium H_2O and P–T conditions determined by the inverse model, sphene saturation is partially limited by TiO_2 content.